

Fundamental Investigation of the Interface Formation of Multi-material Additive Manufactured 316L-CuSn10 Structures



ALASDAIR BULLOCH, ANDY HARRIS, ALLIN GROOM, AMANDA CRUCHLEY, CHRISTOPHER J. TUCK, and MARCO SIMONELLI

The combination of the design freedom offered by metal additive manufacturing with multi-metallic capabilities offers the opportunity to fabricate new advanced components for a number of high value industries. However, a deep understanding of the interface is required to be confident in their functionality. In this study, a methodical approach is developed to study the interfacial properties of a combined 316L and CuSn10 structure. A Schaeffler Aerosint selective powder deposition recoater is used for the co-deposition of 316L and CuSn10 powders. The use of XRD depth profiling to capture data throughout the interface is related to microscopy to elucidate the mechanisms associated to the interface formation, giving insights into how 316L and CuSn10 bond not previously reported. These observations are coupled to thermodynamic modelling to explain the nature of the hot cracks which form at the interface. This methodology provides a detailed insight into the interface of a multi-metallic additive manufactured part, emphasizing the importance of a stepped approach to phase identification and its value to support thermodynamic calculations. Consequently, following this methodology for other material combinations will provide a deep understanding of the interfacial properties aiding in the production of functional components.

<https://doi.org/10.1007/s11661-025-07817-1>
© The Author(s) 2025

I. INTRODUCTION

COMBINING metals with distinct properties has gathered a great amount of interest in recent years.^[1-5] In particular, the combination of the high conductivity of copper, and the mechanical strength and corrosion resistance of stainless steel could find applications as heat exchangers, and tool moulds. Several methods have been investigated for combining steel and copper, such as laser welding,^[6] electron beam welding,^[7] and solid state joining processes like diffusion bonding^[8] and friction stir welding.^[9] However, these techniques are limited in the geometry of the overall structure which can be manufactured and the complexity of the

interfaces achievable. Additive manufacturing (AM), which builds the structure in a layer-by-layer manner, is able to produce parts of highly complex geometry.^[10] Adding the multi-material capability to AM enables three dimensional deposition of each metal and as such, complex interfacial geometries can be produced to improve the bond strength.^[11] The respective properties of the dissimilar materials can also be spatially distributed throughout the part as required. Additionally, it reduces the number of manufacturing steps needed, as both the production of the individual metals and the joining are completed simultaneously.

Laser powder bed fusion (LPBF) is a type of AM which offers considerable design freedom.^[10] As such, several methods have been developed to deposit multiple materials in LPBF machines.^[12] Methods of multi-material LPBF include for example, a nozzle-based approach^[13] or with the use of multiple hoppers.^[14] One of the few commercially available solutions is the selective powder deposition (SPD) recoating unit developed by Schaeffler Aerosint.^[15] This multi-material deposition technique uses a vacuum to adhere a thin layer of powder to a mesh drum. The powder is then selectively deposited *via* a matrix of valves within the drum which locally offsets the vacuum. Using multiple drums allows for multiple materials to be deposited.

ALASDAIR BULLOCH, CHRISTOPHER J. TUCK, and MARCO SIMONELLI are with the Centre for Additive Manufacturing, University of Nottingham, Nottingham NG8 1BB, UK. Contact e-mail: Marco.Simonelli@nottingham.ac.uk ANDY HARRIS and ALLIN GROOM are with the Autodesk Research, Autodesk Ltd., 6 Agar Street, London WC2N 4HN, UK. AMANDA CRUCHLEY is with the Manufacturing Technology Centre, Ansty Park, Coventry CV7 9JU, UK.

Manuscript submitted October 14, 2024; accepted April 28, 2025.

This enables co-deposition of multiple powders during the LPBF process, and therefore does not require the build to be paused and powders swapped for a change in material. This system has been used to combine steel and copper alloys to create tool steel bodies with increased thermal diffusivity^[16] and multi-material electric motors,^[17] effectively proving its capability of fabricating functional multi-material structures of steel and copper alloys. However, due to the method of depositing multiple powders, this system may find it challenging to produce highly complex parts due to the deposition resolution of $500\ \mu\text{m}^2$ and any misalignment between the laser source and the powder pattern deposited. Additionally, there is significant mixing of the unmelted powders, limiting the reusability of the deposited powders. Key to enabling the successful fabrication of functional multi-material structures beyond prototypes is a detailed understanding of how the dissimilar metals are brought in contact, or in other words, the formation of the interface, specifically at the point of manufacture.

Several studies on the LPBF of combined copper and steel alloy structures have been conducted by either switching material at some point throughout the experiment with a standard machine,^[18–20] or using a dedicated multi-material setup.^[21–24] However, only a dedicated multi-material setup is capable of producing parts with different materials deposited within the same layer, and therefore able to produce complex functional multi-material parts. Hence, studying the interface produced by a dedicated multi-material machine is of greater value.

Many of these studies have observed the formation of fine equiaxed grains at the bimetallic interface,^[18–21] which is typically attributed to the segregation of the alloying elements as the alloys mix, and the higher thermal conductivity of the copper alloy.^[22,25] Additionally, segregation of the austenite-stabilising nickel content in stainless steel results in the development of ferrite at the interface.^[23,26,27] Cracking has also been found to occur at the interface in either deposition order^[28,29] driven by the embrittlement effect of liquid copper on austenitic stainless steel,^[23,27,30] and the difference in thermal and physical properties of iron and copper.^[31,32] This occurs across other fusion processes, such as laser welding,^[6] electron beam welding,^[7] and directed energy deposition.^[33] On the other hand, solid state joining processes, such as diffusion bonding^[8] and friction welding,^[9,34,35] reliably produce crack-free joints between stainless steel and a copper alloy. This hints that the nature of the cracking at the interface is likely related to solidification.

As cracking is common among combined iron (Fe) and copper (Cu) systems using LPBF, several studies have been conducted to understand the cause of this and the influence of the Fe:Cu ratio. Mechanical mixing of elemental Fe and Cu powders to produce alloys can result in a non-homogenous distribution of the Cu throughout the Fe matrix, forming Cu clusters which are unable to form a single solution with the Fe matrix. Instead, they form a Cu liquid between the Fe grains and initiate cracking during solidification.^[36] The cracking can be reduced by reducing the Cu content, thereby

reducing the amount of Cu clusters. However, even at low wt pct Cu (10 wt pct), these clusters can still form,^[36] therefore a different technique is needed to ensure a uniform distribution of the Cu into the Fe matrix. Using a prealloyed Fe10Cu alloy, with careful selection of process parameters, was shown to prevent cracking. However, cracks can still form with excessive laser power.^[37]

It is important to consider the cracking behavior at the interface of combined Fe and Cu alloys also. Wen *et al.*^[27] applied a compositional gradient between 316L and CuSn10, increasing the amount of CuSn10 in increments of 10 wt pct. The study observed that samples between 10 and 40 wt pct CuSn10 produced hot cracks. The exact composition which onsets hot cracks is not determined, however, the lowest content of CuSn10 (10 wt pct) examined provided the highest crack density. Similarly, Tucker *et al.*^[38] studied the effect of 1 to 10 particle percent (pt. pct) of CuCrZr contamination on the microstructure of 316L, observing hot cracks even at the 1 pt. pct of CuCrZr. Similar to the study by Zafari *et al.*,^[36] the hot cracks occur in the Cu-rich regions.

Conventional processes have also studied the effect of copper contamination on steel, with cracking in 1045 steel found to generally occur above 0.21 wt pct Cu, due to copper enrichment along grain boundaries.^[39] A composition of mild steel with 0.3 wt pct Cu was shown to produce hot cracks, with a liquid Cu enriched phase identified at the grain boundaries near the cracks. The addition of 0.15 wt pct Ni to the alloy has been found to prevent these hot cracks by alloying with the Cu content and preventing the formation of the detrimental Cu-rich liquid.^[40] These two studies outline the exceptionally low content of Cu contamination needed to form hot cracks in steel, and the role of Ni which can prevent them.

Regardless, several approaches have been taken to prevent the cracks from forming. A study on the influence of process parameters on the interface^[21] found high energy input causes vertical microcracks and insufficient energy leads to lack of fusion defects which form horizontal cracks. Whereas a sweet spot in between produces a defect-free interface. However, the study lacks an in-depth evaluation of the cause of the cracking. Using a nickel-based alloy as an interlayer has been shown to successfully prevent cracking from occurring at the interface.^[41] However, this approach increases the complexity of multi-material LPBF as it requires an additional (third) material to be deposited and can cause greater susceptibility to powder contamination across the alloys. A band of ferrite can be intentionally induced at the interface to suppress copper penetration into the austenite grain boundaries and prevent cracking.^[26] This technique adds an additional chemical process into the fabrication in order to induce the ferrite band, increasing the complexity of multi-material LPBF. Chemical grading of the composition between the two alloys can also be effective,^[27] but it will also increase the complexity of multi-material deposition. Additionally, cracking has shown to be alleviated in post-processing through hot isostatic pressing (HIPping).^[42] However, this requires an additional

(expensive) process after fabrication and introduces size limitations.

The recoater developed by Schaeffler Aerosint, a dedicated multi-material setup, has been used for several studies. The study on the combination of M300 tool steel and CuCrZr by Li *et al.*^[16] provides evidence of hot cracks and porosity at the interface, in both deposition sequences. Regardless of these defects, the thermal diffusivity of the multi-material body increases by around 70 to 100 pct when compared to a pure M300 sample. Optimisation of process parameters to remove lack of fusion pores at the interface when depositing M300 on CuCrZr, improved the thermal diffusivity, whereas performing the same process optimisation in the reverse deposition has little effect on the thermal diffusivity. The authors attribute this to the high angle boundaries of the microstructure at the interface due to the lattice mismatch between the body centred cubic (BCC) structure of M300 and the face centred cubic (FCC) structure of CuCrZr. This study presents key insights into a multi-material sample with immiscible alloys, providing evidence that thermal diffusivity can be increased by the introduction of a conductive alloy. However, the study uses two alloys of a common microstructure, and porosity due to lack of fusion does not occur at the interface. The 316L and CuSn10 combination of this study is therefore inherently unique in its direct focus on hot cracking without lack of fusion or direct lattice mismatch.

Deillon *et al.*^[42] also used the Schaeffler Aerosint recoater to create vertical and horizontal interfaces of a combined 316L and CuCrZr sample. Cracks are shown to develop in the vertical interface as well as the 316L on top of CuCrZr and CuCrZr on top of 316L horizontal interfaces. Porosity is also evident in the vertical interface. The authors successfully prove that HIPping of the samples will heal the defects, and also outline the formation of a Cu-rich phase in the regions where the cracks likely occurred in the as-built state. The study uses two alloys of a similar crystal structure (FCC), and does identify small quantities of a BCC phase to form at the interface, however there is no in-depth discussion of how this new phase forms. Additionally, there is limited discussion of the mixing at the interface and how it is affected by the deposition sequence.

Several of the studies which gather X-ray diffraction (XRD) measurements of the interface of 316L and CuSn10 directly bonded together, conclude there are no new phases which form regardless of deposition order.^[28,43–45] However, XRD measurements of samples of a mix of both alloys have been shown to produce alpha ferrite (α -Fe), which does not exist in the individual alloys.^[27,46] The discrepancy in the phases identified in the XRD in the literature requires a review of the XRD methodology typically conducted for the interface of these two alloys when they are directly bonded.

In this study, XRD depth profiling is used to capture data throughout the interface of bonded 316L and CuSn10 samples produced using a Schaeffler Aerosint selective powder deposition recoater. This multi-material technology is prone to cross contamination of

powder due to gas flow; however, it is proven to be capable of depositing multiple powders accurately in a single pass over the substrate. Observations of interfacial cracking are accompanied by thermodynamic modelling to explain the nature of the cracking. This is the first study of its kind to identify the presence of α -Fe at the interface of a directly bonded 316L to CuSn10 LPBF manufactured structure. Additionally, electron backscatter diffraction (EBSD) is used to identify the morphology of the α -Fe phase that forms at the interface. This study has identified the existence of a potentially detrimental phase at the interface of a directly bonded 316L to CuSn10 sample. As such, future multi-material samples which are directly bonded together should follow the same methodology to identify all existing phases which may be missed otherwise. Therefore, giving confidence in the robustness or fragility of the multi-material components which are produced.

II. MATERIALS AND METHODS

A. Materials

Spherical 316L powder (provided by Carpenter Additive, UK) and CuSn10 powder (supplied by Aerosint SA, Belgium) were used for this study. The chemical composition for each powder was measured using inductively coupled plasma mass spectrometry (Table I). The particle size distribution (PSD) for each were measured using a Mastersizer 3000 (Malvern Panalytical, UK), and the morphology of the powders were analyzed using a Hitachi TM3030 SEM (Hitachi, Japan). The powder morphology and PSD for both alloys are summarized in Figure 1. Both alloy powders are shown to have a near spherical shape with the presence of some fine satellites. Additionally, a gaussian-like distribution of both powders is shown to be present with a PSD of $D_{10} = 19.9 \mu\text{m}$, $D_{50} = 30.8 \mu\text{m}$, and $D_{90} = 47.2 \mu\text{m}$, and $D_{10} = 9.5 \mu\text{m}$, $D_{50} = 21.1 \mu\text{m}$, and $D_{90} = 35.7 \mu\text{m}$ for 316L and CuSn10, respectively.

B. Experimental Setup

Samples were produced using an AconityMI-DI+LPBF machine (Aconity3D GmbH, Germany) which features a 1 kW continuous wave (CW) ytterbium fibre laser (nLIGHT alta), and two 400 W CW ytterbium fibre lasers (IPG Photonics Ltd. UK), all operating at 1070 nm wavelength with a focussed beam spot diameter of 80 μm .

Netfabb Ultimate 2023 (Autodesk Inc.) was used for part creation and slicing of the build file. The multi-material parts were treated as an assembly with each material created as an individual STL file. Each STL file was then sliced and hatched as separate CLI files with a shared origin point to ensure materials aligned correctly at the interface. The CLI files were then uploaded to AconitySTUDIO (Aconity3D GmbH, Germany) for build preparation.

An Aerosint SPD recoater (Aerosint, Belgium) was used as the multiple powder delivery system. This deposition unit allows for both powders to be simultaneously deposited within one pass over the substrate. Therefore, when compared to other proposed systems, it has a coating rate which is relatively close to conventional single material LPBF.^[47] The system comprises two cylindrical drums with a wire mesh coating (10 μm nominal sieve opening), a negative pressure is held within these drums to hold a layer of powder (between 200 and 250 μm thick) to the mesh of the drum. Within each drum is a matrix of nozzles facing downwards near the surface of the mesh. The matrix is made up of 4 rows of 48 nozzles, slightly offset such that each individual nozzle has a unique placement in the y axis giving a powder deposition resolution of 500 μm^2 . As the recoater passes over the substrate, both drums rotate whilst the valves release argon through the mesh to selectively deposit powder from each drum within the regions outlined in the sliced STL file. 316L powder is used to fill in the remaining area around the build plate. A levelling blade and vacuum then follow the drums to ensure a uniform 40 μm powder layer. Argon flows parallel to the y -direction. A schematic detailing the method by which the Aerosint deposits multiple powders in a single layer is shown in Figure 2. The capability of the Aerosint SPD recoater is demonstrated through the example combined 316L and CuSn10 parts shown in Figure 3, highlighting the ability to spatially distribute the individual materials both within the same layer and in subsequent layers.

Prior to fabrication of samples for analysis, alignment of the laser scanners with the powder pattern was ensured. An example layer of both powders is deposited, and the contours of the sliced files are scanned using the 1 kW laser. The offset between the scanned contour and the contour of the pattern deposited is measured, and adjustments to the x and y axis offset values are corrected.

C. Experimental Procedure

Both alloy powders were dried at 70 $^{\circ}\text{C}$ for 16 hours before the build. Rectangular samples with an 8 mm^2 footprint and a total of 2 mm build height were first deposited. On top of this, the other alloy was then deposited in the form of an 8 mm^2 footprint with a height of 2 mm. Both orientations were fabricated directly on to the substrate. The samples were fabricated using parameters suggested by Aerosint, this consists of a stripe hatching scan strategy with the parameters for each alloy outlined in Table II under an Argon atmosphere with a 90 deg hatch rotation between each layer. The area energy density is the calculated energy density delivered by the laser during a single scan track, using the power (P), scan speed (v) and spot diameter (d) calculated by:

$$\text{Area energy density} = \frac{P}{v * (\pi * (\frac{d}{2})^2)}$$

An oxygen level below 500 ppm was set to begin the build, as the build progressed the oxygen level dropped further to below 100 ppm. The samples were then wire cut off the build plate for analysis.

To understand how the composition changes and the microstructure evolves in relation to the change in material, a second set of 316L-CuSn10 rectangular samples were created. This time the upper material was deposited for ten layers, allowing for the point at which the material deposition was changed to be quantified (to within a couple of layers) in post-processing. This was conducted on both deposition sequences.

D. Material Characterization

Prior to metallurgical characterization, the samples were sectioned parallel to the build direction (BD), mounted, ground, and polished with a final step of polish with colloidal silica. A Nikon eclipse LV100ND (Nikon Corporation, Japan) optical microscope was used for capturing optical micrographs. A JEOL 7100 field emission gun scanning electron microscope (FEG-SEM) (JEOL, Ltd., Japan) equipped with a Nordlys-Max3 electron backscatter diffraction (EBSD) detector was used to capture secondary electron and backscatter electron images, and to collect chemical composition and crystallographic data of the specimens. The EBSD data were collected using an accelerating voltage of 15 kV and a step size of 0.35 μm . A Hitachi TM3030 SEM was used to capture secondary electron micrographs of the individual alloys. These micrographs were used to measure the area of the pores *via* ImageJ software (National Institutes of Health) and calculate the relative density.

The second set of rectangular samples were used to quantify the change in composition across the interface and to identify the presence of new phases which develop at certain regions within the interface. A JEOL 7100 FEG-SEM is used to quantify the change in composition across the interface. For this, 12 scan lines, spaced out equally from each other by 100 μm , are aligned parallel to the build direction. This method is reflected in the Appendix Figure 12, where each scan line (represented by the dashed white arrow) begins roughly around the top of the sample and continues in the negative build direction, crossing the interface. Every 10 μm along each scan line, a localised composition is recorded. The recording at each ten micron step along all of the scan lines are then combined to create an averaged composition value throughout the build direction. X-ray diffraction (XRD) measurements were taken at 50 μm intervals along the build direction. This was achieved by measuring the initial height of a rectangular sample with a set of callipers then, using a combination of grinding with P2500 paper and polishing, the height of the rectangular sample was carefully reduced to the desired build height. For example, to reach the build height at which the material changed, referred to in this paper as the transition region, the rectangular sample would be reduced in height by 400 μm (approx. 8 to 10 layers). The phases present at each section were identified using a Bruker D8 Advance Da Vinci with a

Table I. Measured Chemical Composition of 316L and CuSn10 Powder Used in This Study

Material	Element [Wt Pct]												
	C	Cr	Cu	Fe	Mn	Mo	N	Ni	O	P	S	Si	Sn
316L	0.02	17.80		bal.	0.96	2.30	0.07	12.60	0.03	0.01	0.01	0.66	
CuSn10			bal.										10.32

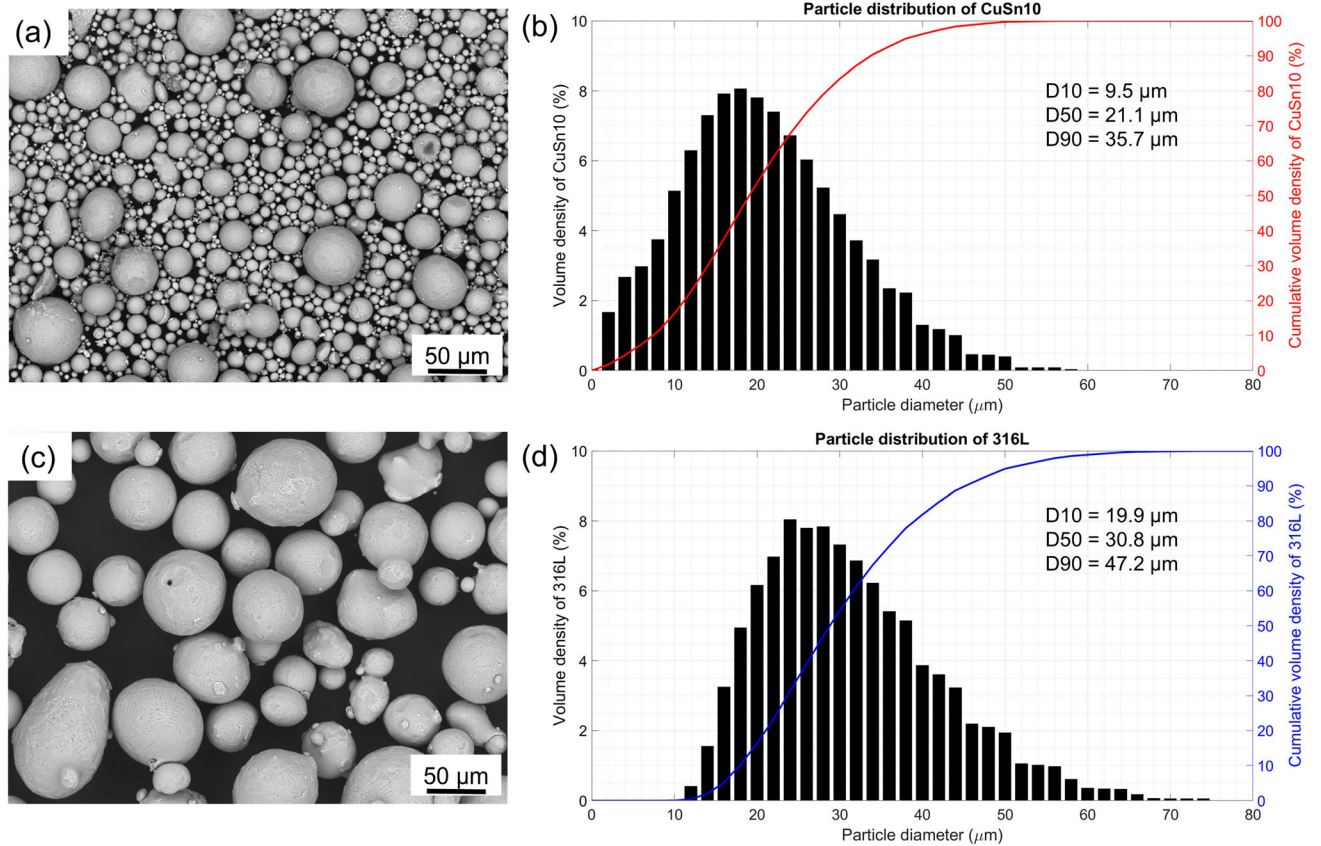


Fig. 1—Characterization of the powder used in this study, (a) scanning electron microscope (SEM) image showing the morphology of the CuSn10 powder, (b) particle size distribution of the CuSn10 powder, (c) SEM image of the 316L powder, and (d) particle size distribution of the 316L powder.

Lynxeye 1D detector. Data were gathered with a step size of 0.02 deg and a step time of 3s scanning in a range of $2\theta = 20$ to 100 deg. Diffraction peaks were then identified using Diffrac.EVA and the ICDD database PDF-2 2021. Fluorescence occurs when copper is combined with iron samples. This results in low penetration depth of the x-rays, with one study calculating the penetration depth to be about $6 \mu\text{m}$.^[48] Based on the study by Mos *et al.*^[48] it is assumed that the penetration depth of the x-rays for the samples in this study increases from 5 to $20 \mu\text{m}$ between the 2θ range of 20 to 100 deg.

E. Thermodynamic calculations

The CALculated PHase Diagram (CALPHAD) method is employed using Thermo-CalcTM version 2022b^[49] with the TCFE9 and SSOL5 thermodynamic databases to predict the solidification of the melt pool at the interface. Calculations of the solidification path of various combinations of 316L and CuSn10 are performed using the classic Scheil method. Weightings are applied to the compositions outlined in Table I.

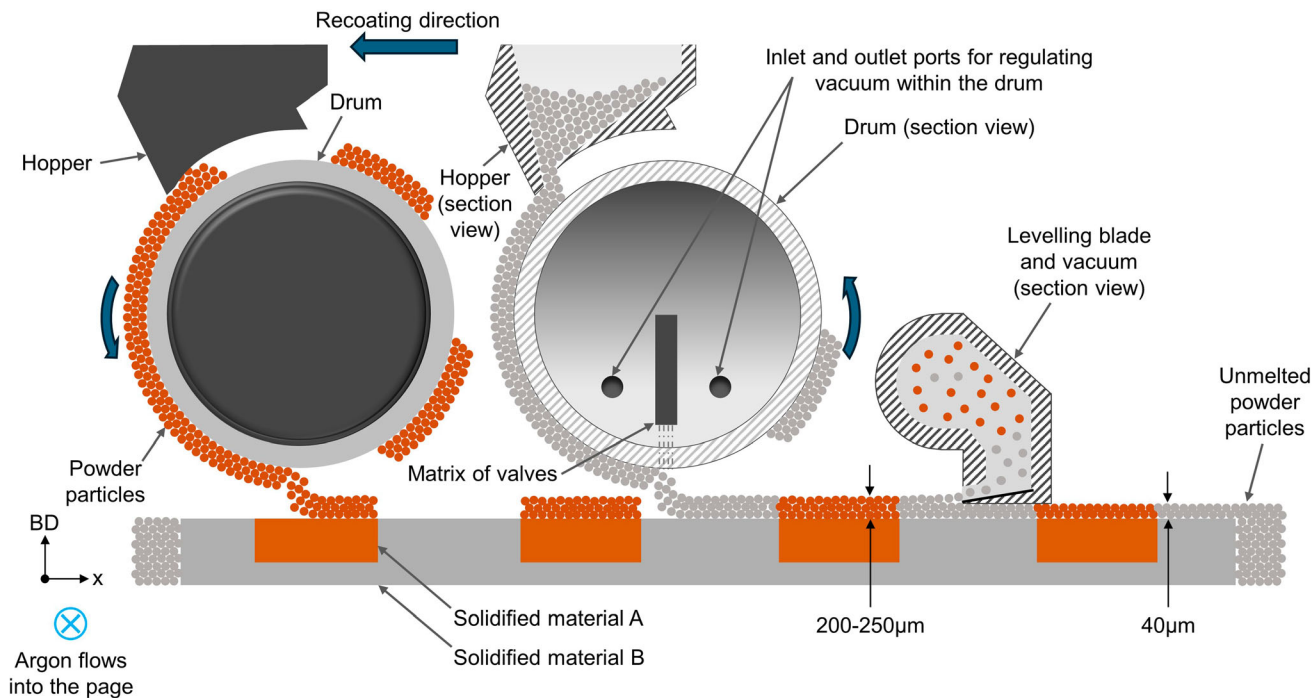


Fig. 2—Schematic of the device used to deposit two distinct metal powders in a single recoating layer. The device recoats from the left to the right, with both drums rotating counterclockwise. Argon flows parallel to the y direction.

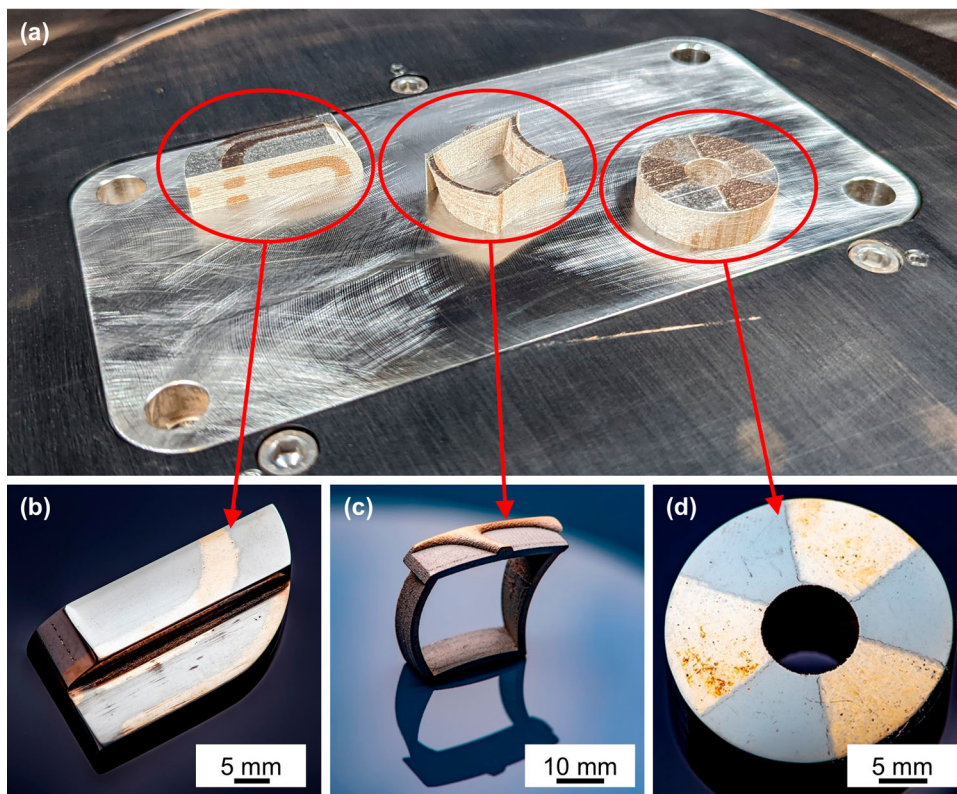


Fig. 3—Example bimetallic 316L-CuSn10 parts produced using the Aerosint SPD recoater. (a) shows three demonstration parts in the as-built state on the build plate. (b) through (d) are each demonstration part after being wire cut off the build plate and polished.

Table II. Parameters Used for Processing 316L and CuSn10 Powder in This Study

Material	Laser Power (W)	Scan Speed (mm/s)	Hatch Distance (μm)	Spot Diameter (μm)	Layer Thickness (μm)	Hatch Rotation Angle (Deg)	Stripe Width (mm)	Area Energy Density (J/mm^2)
316L	150	600	80	80	40	90	10	50
CuSn10	200	500	120	80	40	90	5	80

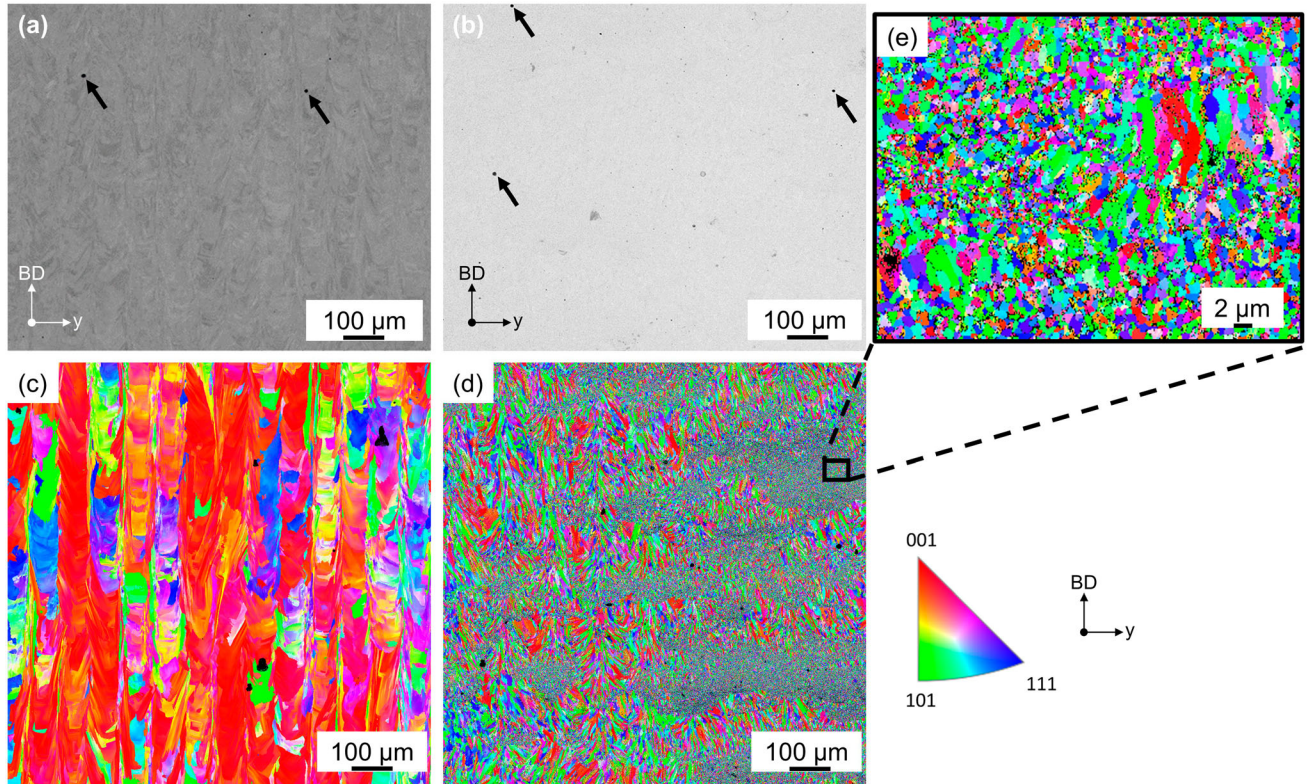


Fig. 4—Single material characterization of the parameters outlined in Table II. (a) and (b) are optical micrographs of sections of 316L and CuSn10, respectively, (c) and (d) are the inverse pole figure (IPF) maps of 316L and CuSn10, respectively, and (e) is a high magnification IPF map of the region outlined in (d). The inset shows the IPF key with the (001) orientation aligned to the build direction (BD).

III. RESULTS

A. Microstructural Evolution in the Individual Alloys

To understand the suitability of the parameters suggested by Aerosint (shown in Table II), single material cubes were printed and assessed for their density. Example optical micrographs showing the sectioned surface of a pure 316L and pure CuSn10 sample are shown in Figures 4(a) and (b). Density calculations show the parameters produce a relative density of 99.9 pct and 99.5 pct for 316L and CuSn10, respectively. Circular pores are highlighted by black arrows in Figures 4(a) and (b).

The microstructure of each alloy is presented by the inverse pole figure (IPF) maps shown in Figure 4 where the inset IPF color key represents the (001) orientation aligned with the build direction (BD). Figure 4(c) represents the microstructure of 316L with columnar

grains aligned along the build direction. Figure 4(d) represents the microstructure of CuSn10, which consists of a mix of columnar grains and fine equiaxed grains, as displayed in the high magnification IPF map shown in Figure 4(e). Similar columnar microstructures for each of the single alloys are observed in a study of 316L and CuSn10 by Wen *et al.*^[27] EDS maps of the copper content in the region shown in Figure 4(c) is shown in the appendix Figure 13(a), and of the iron content in the regions shown in Figure 4(d) and (e) are shown in the appendix Figures 13(b) and (c), respectively. These indicate the contamination of opposing materials into each alloy, with more pronounced contamination of iron in the CuSn10 sample. This iron contamination is found in the regions containing the fine equiaxed grains. It has been illustrated that the addition of iron to a copper matrix of LPBF produced samples transforms the columnar grains of pure copper into fine equiaxed

grains of a similar scale to those observed in Figure 4(e).^[50]

The inert atmosphere is regulated by an argon gas flow, and the direction of this gas flow is perpendicular to the recoating direction. Therefore, with reference to Figure 2, the argon gas flow is travelling into the page. As is outlined in the study on developing guidelines for creating bimetallic structures with the Aerosint recoater,^[51] the gas flow can interrupt the particles as they drop on the bed and result in contamination of the other material. It is also possible that the gas flow disturbs the particles on the drum, lifting it onto the other drum. For example, the larger 316L particles on the right drum in Figure 2 could be interrupted by the argon gas flow and fall onto the drum on the left, resulting in contamination of the drum with the CuSn10 powder.

B. Deposition of Multi-material Samples and Characterization of the Interface

Optical microscope images of the resulting interface when depositing 316L on top of CuSn10 and depositing CuSn10 on top of 316L are shown in Figures 5(a) and (b), respectively. The build direction is aligned with the z axis, and the hatching direction of the first layer of the upper material is parallel to the x axis.

Deposition of 316L on top of CuSn10 results in significant cracking aligned with the build direction, as shown in the y -BD section of Figure 5(a). In comparison, cracking is less prominent when depositing CuSn10 on top of 316L, as shown in Figure 5(b). Bai *et al.*^[28] and Chen *et al.*^[29] observe similar behavior. This paper concentrates on the y -BD section of both deposition sequences as cracking is mostly observed in this section for both orientations.

Secondary electron images of the y -BD interface for the different deposition sequences are shown in Figure 6. It is evident that at least two distinct phases are observed, one with a dark contrast and the other with a light contrast. Based on the deposition orders of

Figures 6(a) and (d), the dark and bright contrast phases are associated with 316L and CuSn10, respectively.

A relatively sharp interface forms when depositing 316L on top of CuSn10, shown in Figure 6(a), with cracking occurring only in the 316L region of the interface and coming to an end at the boundary of the sharp interface, as shown by Figure 6(b). The cracks in the 316L region tend to align along the build direction and appear to be intergranular as the propagation either comes to a stop or changes direction once it encounters a grain, this is highlighted by the white dashed arrows in Figure 6(c).

Figure 6(d) indicates that when the sequence is reversed (depositing CuSn10 on top of 316L), the interface morphology is noticeably different with deep melt pools appearing evident, outlined by the yellow curves, and a greater amount of mixing of the two alloys makes it difficult to identify the point at which the sample switched materials (or, in other words, to identify the nominal interface between the dissimilar materials). Figure 6(e) shows the presence of cracks within only the 316L region of the interface which penetrate normal to the melt pool boundaries (indicated by the solid white arrows) and then continue along the build direction. The cracks in this deposition sequence differ from those shown in Figure 6(a) as they are filled with a brighter phase. The high magnification image shown in Figure 6(f), displays the existence of the two distinct phases distributed across the interface. The white solid line highlights an island of the bright phase encased by the dark phase, with smaller circular islands of the dark phase existing within the bright phase island. These small circular dark phase regions are also shown to be distributed throughout the bulk of the bright phase as shown by the dashed white arrow. This is attributed to the metastable liquid phase separation which is thought to occur in the Fe-Cu binary system provided the alloyed melt pool is undercooled below the metastable miscibility gap.^[25,52,53]

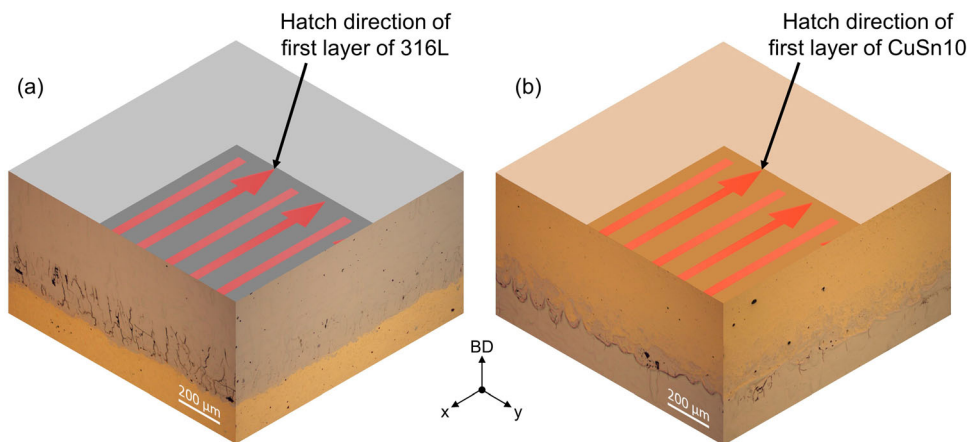


Fig. 5—Optical microscope images of the interface between 316L and CuSn10 (a) 316L deposited on top of CuSn10, (b) CuSn10 deposited on top of 316L. The hatching direction is parallel to the x axis in both deposition sequences for the first layer of the upper material, subsequent layers are then rotated by 90 deg. The build direction is aligned with the z axis.

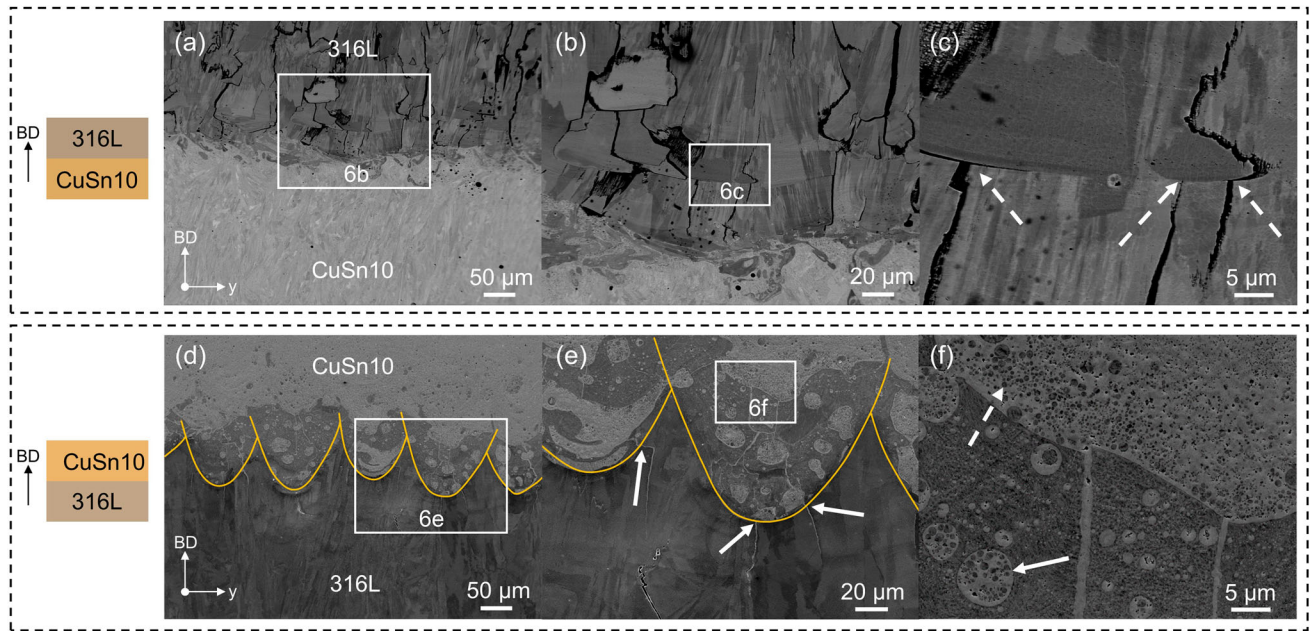


Fig. 6—Secondary electron images of the interface of both deposition sequences (*a* through *c*) are $\times 200$, $\times 500$, and $\times 2500$ magnification of 316L deposited on top of CuSn10, respectively, (*d* through *f*) are $\times 200$, $\times 500$, and $\times 2500$ magnification of CuSn10 deposited on top of 316L, respectively (Color figure online).

To understand the nature of the phases that have formed at the interface, EDS was conducted on both deposition sequences. Backscatter electron images of the interface when 316L is deposited onto CuSn10 is shown in Figure 7(a), with CuSn10 deposited onto 316L is shown in Figure 7(d). An enlarged portion of each is outlined in Figures 7(b) and (e), respectively.

Figures 7(b) and (e) reflect the difference in mixing mode based on the deposition order. A banding effect of the bright contrast phase within the dark contrast phase, highlighted by the solid yellow arrows in Figure 7(b), develops over a narrow range of about $60 \mu\text{m}$ in the build direction when depositing 316L onto CuSn10. Whereas deposition of CuSn10 onto 316L results in circular structures of the dark contrast phase of a variety of diameters dispersed throughout the bright contrast phase, such as those outlined by the solid yellow arrows in Figure 7(e), and occurring over a wider range of about $200 \mu\text{m}$ in the build direction (Figure 7(d)). A high magnification image of the interface and the related EDS maps (of the main constituent elements of each alloy) of 316L on top of CuSn10 and of CuSn10 on top of 316L are shown in Figures 7(c) and (f), respectively. As occurred in Figure 6(f), brighter phase regions encased by the darker phase occur in Figure 7(c1) (as highlighted by the dashed yellow arrows). Circular regions of the dark phase within the bulk of the bright phase also occur in both Figures 7(c1) and (f1), indicated by the solid yellow lines. In both deposition orders, the isolated dark circular regions exist down to the submicron scale. The respective positions of these structures in the EDS maps of the main elements for both alloys, iron (Figures 7(c2) and (f2)) and copper (Figures 7(c3) and (f3)), show that the bright phase is copper-rich and the dark phase is iron-rich.

The EDS maps of the other main constituent elements of this system (chromium, tin, and nickel) for 316L on top of CuSn10 and CuSn10 on top of 316L are shown in Figures 7(c4-6) and (f4-6), respectively. Both chromium and tin reflect the same trend as the iron and copper, respectively, representing the steel and copper alloys. Conversely, the EDS maps of nickel (Figures 7(c6) and (f6)), are aligned with the copper and tin and show a localized depletion of nickel content in the phase of darker contrast.

The evolution of the composition across the interface when depositing 316L on top of CuSn10 and when depositing CuSn10 on top of 316L is shown in Figures 8(a) and (b), respectively. The transition region is near the middle of each of the micrographs, and as such, it is evident that the mixing of the alloys is affected by the deposition sequence. When depositing 316L onto CuSn10, mixing occurs primarily above the point at which materials change (Figure 8(a)), indicating limited remelting of the base metal (CuSn10). In contrast, Figure 8(b) shows that deposition of CuSn10 onto 316L results in deep penetration into the base metal (316L), and the mixing of the two alloys occurs largely below the layer in which the materials change (at least nominally from design). Additionally, Figure 8(b) displays jagged curves for the iron and copper content within the mixing region, indicating that the significant mixing of the two alloys within the melt pool is widely dispersed throughout the depth of the melt pool. This stands in stark contrast to the more linear gradient in composition shown in Figure 8(a).

The phase map for the regions of the interface outlined by the white box in Figures 8(a) and (b) are shown in Figures 9(a) and (c), respectively. Within the mixing region in both deposition sequences, a BCC

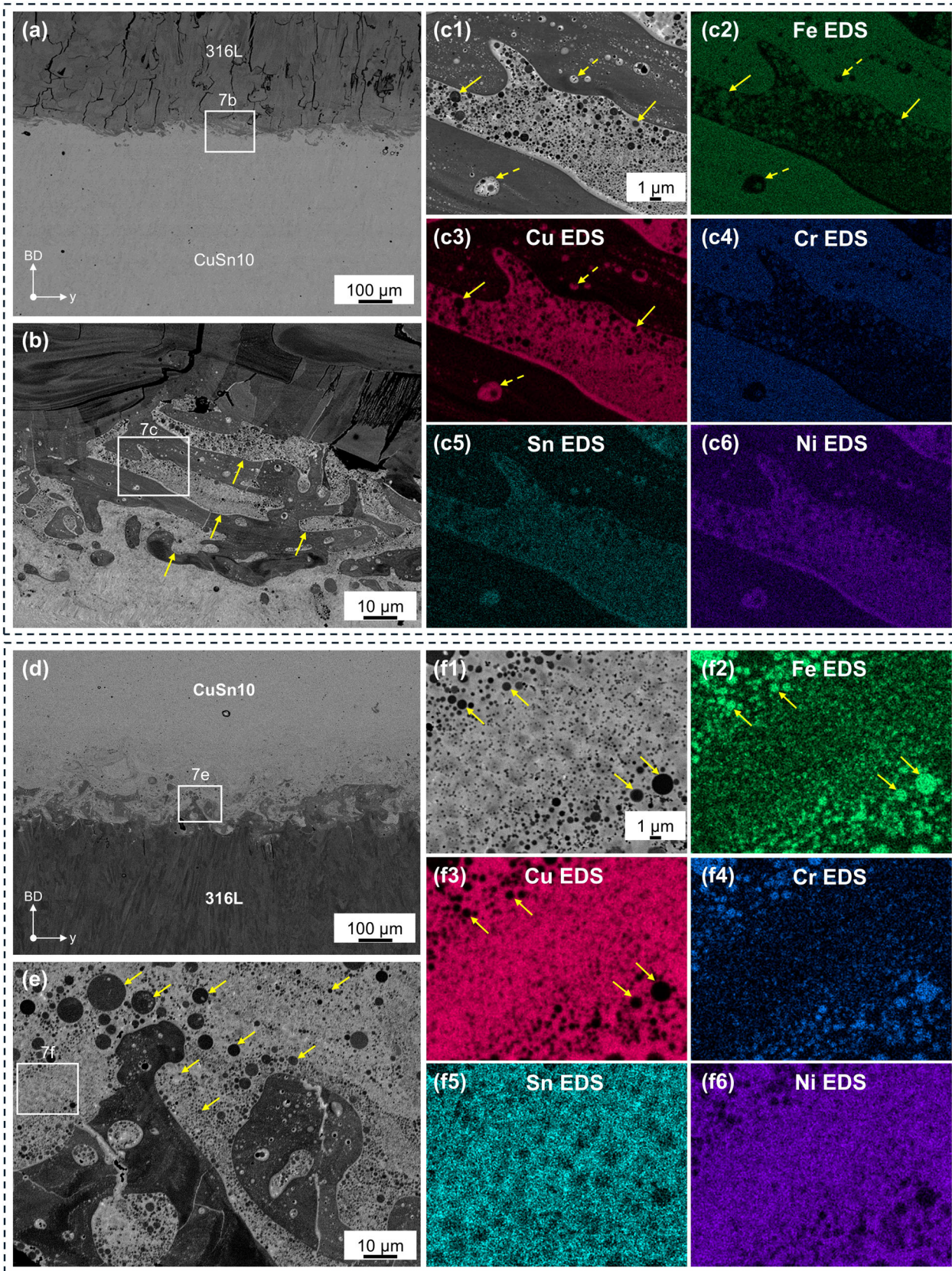


Fig. 7—Backscatter electron images of the interface, (a through c1) are $\times 200$, $\times 1000$, and $\times 5000$ magnification of 316L deposited on top of CuSn10, respectively, (c2 through c6) are the corresponding EDS maps for (c1). (d through f1) are $\times 200$, $\times 1000$, and \times magnification of CuSn10 deposited on top of 316L, respectively, (f2 through f6) are the corresponding EDS maps for (f1) (Color figure online).

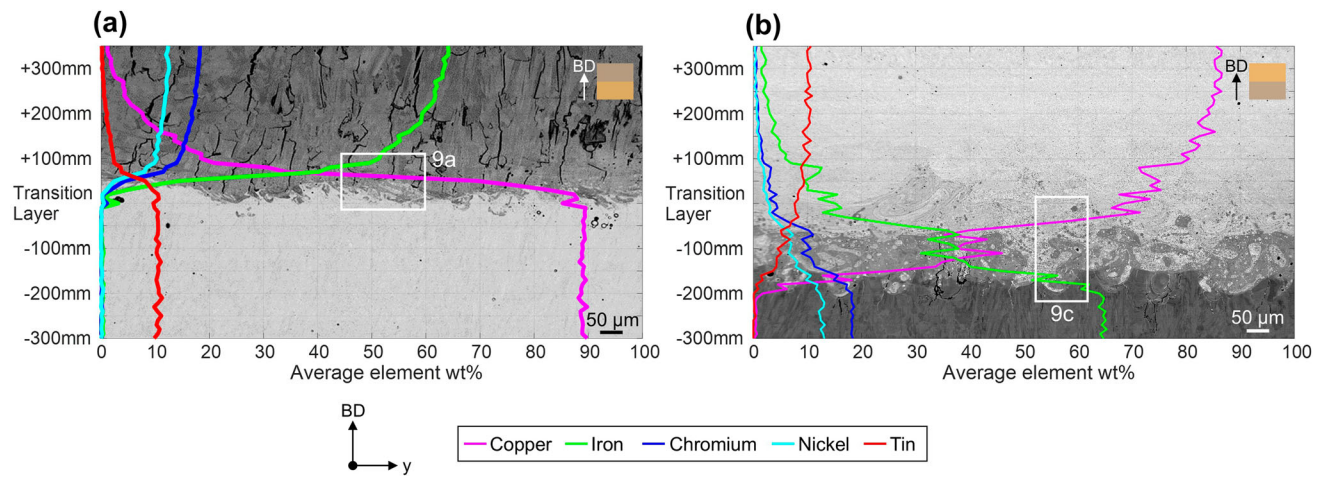


Fig. 8—Backscatter image of the interface with the average change in composition overlaid, (a) 316L on top of CuSn10, and (b) CuSn10 on top of 316L. A schematic at the top right of each micrograph displays their respective build sequence.

phase develops. This BCC phase is distributed over a greater distance in the build direction when depositing CuSn10 on top of 316L (Figure 9(c)), compared to the opposite deposition order, reflecting the increased mixing region shown in Figure 8(b). Additionally, the BCC phase forms as bands when depositing of 316L on top of CuSn10, whereas deposition of CuSn10 on top of 316L leads to a wide distribution of circular-shaped islands of the BCC phase (as highlighted by the yellow arrows in Figure 9(c)). Figures 9(b) and (d) display the XRD measurements for both of the individual alloys as well as the regions labelled in Figures 9(a) and (c), respectively. The surface which was scanned for the regions labelled “Transition region”, “Region 1”, and “Region 2” in Figure 9(b) are shown in Supplementary Figure 14, as an example of how the samples were prepared for the XRD.

The XRD patterns of 316L confirms the presence of austenite (γ -Fe), as is observed in existing studies.^[54,55] The XRD patterns of CuSn10 displays the presence of α -Cu and β -Cu(Sn), matching the patterns recorded in.^[56,57] The XRD patterns of the regions throughout the interface of both deposition sequences indicates the presence of the phases from the individual alloys along with a new phase identified as α -Fe, a BCC phase. Similar studies gathering XRD measurements on the interface between 316L and a copper alloy do not reflect the presence of α -Fe.^[28,43–45] On the other hand, Wen *et al.*^[27] applied a compositional gradient by adding CuSn10 to 316L in steps of 10 pct over a spatial distance. At each 10 pct increment, an XRD measurement was taken revealing the presence of α -Fe in combinations with > 40 pct CuSn10 content. This indicates the importance of using XRD depth profiling measurements of a direct interface between dissimilar metals to capture all of the phases which form.

IV. DISCUSSION

The selective powder deposition recoater developed by Schaeffler Aerosint is proven to be capable of producing bimetallic samples of 316L and CuSn10 with 3D spatial distribution of the individual alloys, as shown by the demonstration parts in Figure 3. Cross-contamination of the powders is a likely outcome with the technology, causing localised changes to the microstructure of the individual alloys. However, this is as a result of the circulation of argon flow within the chamber during deposition. Turning off the circulation during deposition of the powders would reduce the falling of powders outside of the deposition pattern and prevent cross-contamination.

Understanding if a bimetallic structure is robust requires a thorough understanding of the interface. As such, it is of paramount importance to determine how the alloying elements diffuse across the interface as this, along with the processing thermal history, determines the evolution of the observed microstructure. Diffusion of the alloying elements across the interface can occur in both the liquid and solid state. However, in LPBF, it is typically dominated by diffusion in the liquid state,^[58] with physical mixing of the two alloys induced by the swirling motion of the Marangoni flow. As the melting regime transitions from conduction mode to keyhole mode, the melt pool changes from shallow to deep and narrow due to an increase in energy from the laser source.^[59] Therefore, in keyhole mode, the melt pools penetrate deeper into the underlying material and the material is subjected to more melting-solidification cycles. The increase in solidification cycles throughout the build direction results in repetitive mixing inside the melt pool to occur and creates a wide dispersion of the two materials across the interface, thus leading to a

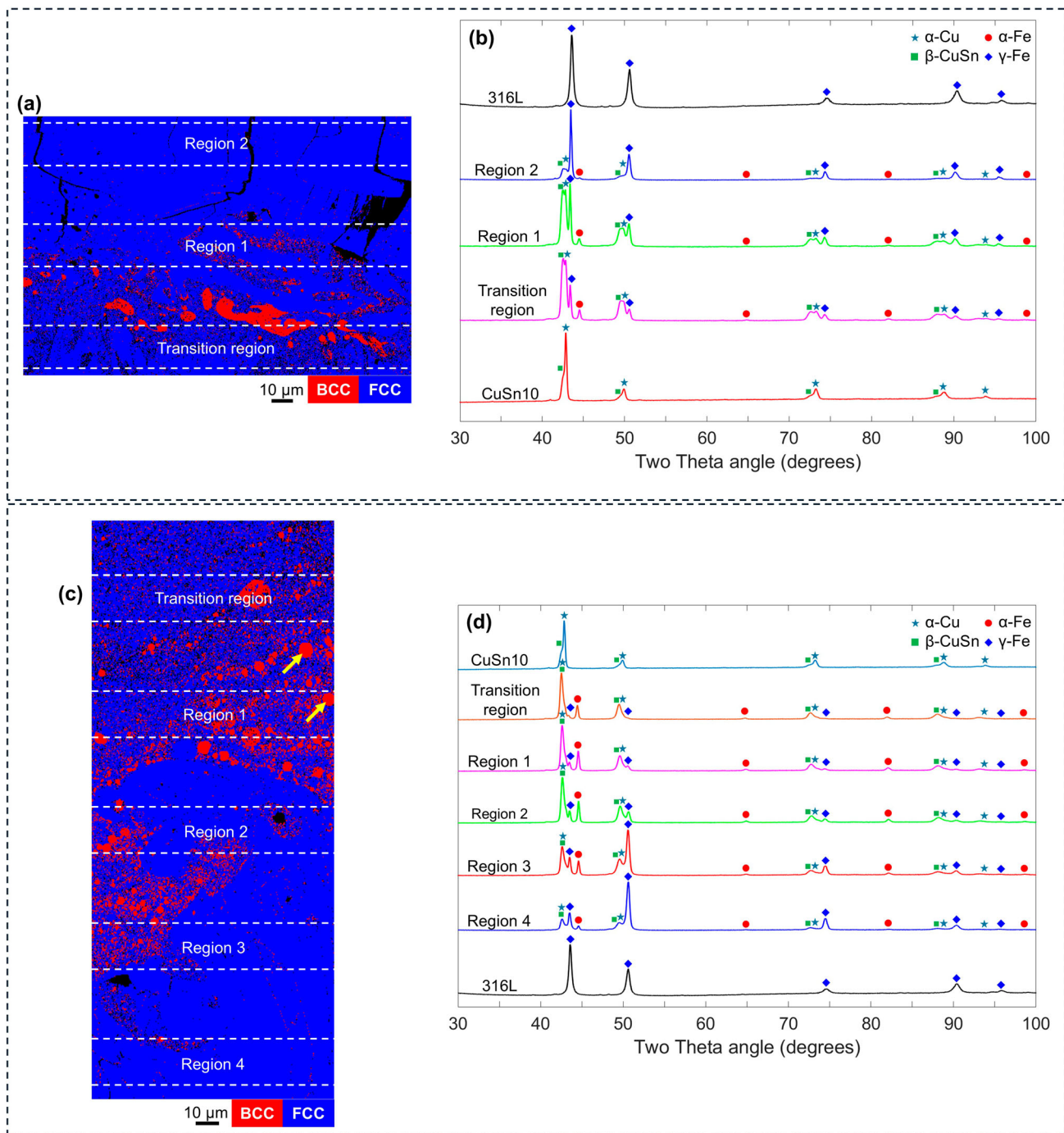


Fig. 9—Evolution of microstructure across the interface. (a, c) show the phase maps of the white boxes highlighted in Figures 8(a) and (b), respectively. (b, d) reflect the XRD measurements of the individual alloys and the regions outlined in (a) and (c), respectively (Color figure online).

wider region for a change in microstructural properties (such as the depletion of nickel in 316L and the formation of ferrite). The formation of austenite or ferrite is known to be affected by composition and thermal conditions.^[60,61] Under equilibrium and low solidification speeds, one could use the concept of the ratio of chromium equivalent and nickel equivalent ($\text{Cr}_{\text{eq}}/\text{Ni}_{\text{eq}}$ ratio) to predict if austenite or ferrite will

dominate during solidification based on a given composition. However, it is well-known that under rapid solidification conditions, the threshold for the $\text{Cr}_{\text{eq}}/\text{Ni}_{\text{eq}}$ ratio can shift.^[60] Considering this, an investigation by Sabzi *et al.*,^[61] determined that a ratio of $\text{Cr}_{\text{eq}}/\text{Ni}_{\text{eq}} > 1.3$ is the threshold for ferrite to dominate during solidification. Applying the methodology followed by Sabzi *et al.* to the two circular-shaped islands of ferrite

highlighted by the yellow arrows in Figure 9(c), the islands both have a Cr_{eq}/Ni_{eq} ratio > 1.3 . This is an indication that the ferrite has formed from the liquid state. Applying the same methodology to the calculated composition of the 316L powder used in this study (Table I) indicates solidification through AF mode (primary austenite solidifying prior to interdendritic ferrite).^[62] In-situ synchrotron XRD measurements of laser melted 316L powder (of identical chemical composition to that used in this study) provides evidence of solidification through the AF mode, with retained ferrite predicted to be between 0 to 2 wt pct.^[63] This quantity of retained ferrite is within a range which can go undetected through conventional XRD measurements, reflected by the XRD measurements of 316L in Figure 9.

As outlined in Table II, a higher area energy density is used to process CuSn10. When processing the first layer of CuSn10 on top of 316L, the increase in area energy density (compared to the previous layer which used process parameters for 316L) results in deeper melt pools as outlined in Figure 6. Keyhole mode is generally defined when the melt pool depth to width ratio (D/W) is greater than 0.55.^[64] The melt pools outlined in Figure 6 were measured to have a D/W ratio between 0.82 and 0.98, hence suggesting that keyhole mode has been reached when depositing CuSn10 on top of 316L. In contrast, the D/W ratio of the reverse deposition sequence is between 0.25 and 0.30 (appendix Figure 15), indicating conduction mode melting. The difference in melting regime may explain the difference in the morphology of the ferrite which forms at the interface. In the case of CuSn10 deposited on top of 316L, heat dissipation is slower due to the lower thermal conductivity of the 316L substrate. Thus, reducing the thermal gradient and allowing the melt pool to be sustained for a greater amount of time. The keyhole melting mode at the interface causes the remelted 316L alloy to be brought up into the CuSn10 layers above in a swirling motion (as can be observed in Figure 7(d)). The alloying elements are able to diffuse over a greater distance across the interface, aided by the turbulence of the Marangoni flow. Subsequently, ferrite forms at many sites throughout the deep melt pools, leading to a scattered distribution of circular-shaped islands of ferrite. The increased melt pool lifetime presumably allows the denser CuSn10, with a lower melting point, to travel deeper into the 316L substrate and backfill intergranular cracks developed in the 316L (Figures 6(d) through (f)). This behavior can be attributed to liquid metal embrittlement (LME),^[65] which has been observed under rapid solidification conditions in the iron-copper binary system.^[25,53,66,67] During LME, copper-rich liquid penetrates the grain boundaries of an FCC crystal structure (in this case austenite) *via* capillary action.^[68] This is also referred to as “copper contamination cracking”.^[30,65,69]

In the reverse deposition order, the CuSn10 substrate acts as a heat sink and dissipates energy faster, through conduction, than a 316L substrate. Therefore, the deposited 316L cools rapidly limiting the time for alloying elements (such as Nickel) to diffuse into the copper, as there is limited time for the molten alloys to

interact. As such, the amount of 316L which solidifies as ferrite is reduced. In addition, the stable melt pools (in conduction mode) at the interface of this deposition sequence reduces turbulence in the melt pool and prevents a scattered distribution of the ferrite. Rather the ferrite forms as planar bands. Additionally, the reduced energy density used for the first layer of 316L on top of CuSn10 as well as the higher reflectivity and higher heat dissipation of the CuSn10 results in limited remelting of the underlying CuSn10 layers. This is reflected by the limited mixing of both alloys occurring above the transition layer as shown in Figures 8(a) and 9(a).

Optical micrographs of both deposition sequences are shown in Figures 10(a) and (e). The IPF map of a section of the interface of both scenarios is shown in Figures 10(b) and (f), the IPF key has the (001) orientation aligned to the build direction. A crack tip of both deposition orders is shown in Figures 10(c) and (g), with the corresponding grain boundary misorientation angle mapped in Figures 10(d) and (h). The cracks are shown to propagate along grain boundaries with high misorientation angles in both deposition orders, which is a common observation in hot cracking.^[70,71] The cracks highlighted by the solid white arrows in Figure 6(e) show a preferential occurrence at the centre of the melt pools, this is also a typical characteristic of hot cracks^[70] and is observed in the cross section of single tracks of CuSn10 deposited on to 316L.^[68]

To further understand the microstructural features (such as the cracks) observed at the interface, it is useful to revert to (pseudo) phase diagrams and thermodynamic calculations. This first requires an interpretation of the phases which form as a result of the mixing of the two alloys. The phases experimentally identified in Figure 9 are used along with the measured composition throughout the interface to calculate the solidification path of various combinations of mixed 316L and CuSn10. A weighting was applied to the composition of both alloys listed in Table I to calculate the solidification path using the classic Scheil model in Thermo-CalcTM. The solidification paths for 95 wt pct/5 wt pct, 90 wt pct/10 wt pct, and 80 wt pct/20 wt pct share of 316L/CuSn10 are shown in Figures 11(a) through (c), respectively. The figure key denotes the phases which develop throughout solidification. Notably, all solidification paths reflect the immiscible state of the molten liquid as there is no single liquid solution. Instead, two distinct liquid phases exist, one rich in iron (L_{Fe}) and the other rich in copper (L_{Cu}). The absence of a single liquid solution explains the precipitation of the iron-rich and copper-rich circular islands throughout the mixing region in Figure 7. Austenite (γ), ferrite (α), and a CuSnMnNi (FCC) and CuSnMn (BCC) phase form throughout solidification. The CuSnMnNi and CuSnMn phases are not highlighted in the XRD plots of Figure 9, however their crystal structures are identical to the phases highlighted in Figure 9 and account for slight peak shift and widening. This is reflected by the enlarged view of the first peaks for both build orientations in Figure 16. Additionally, the formation of the

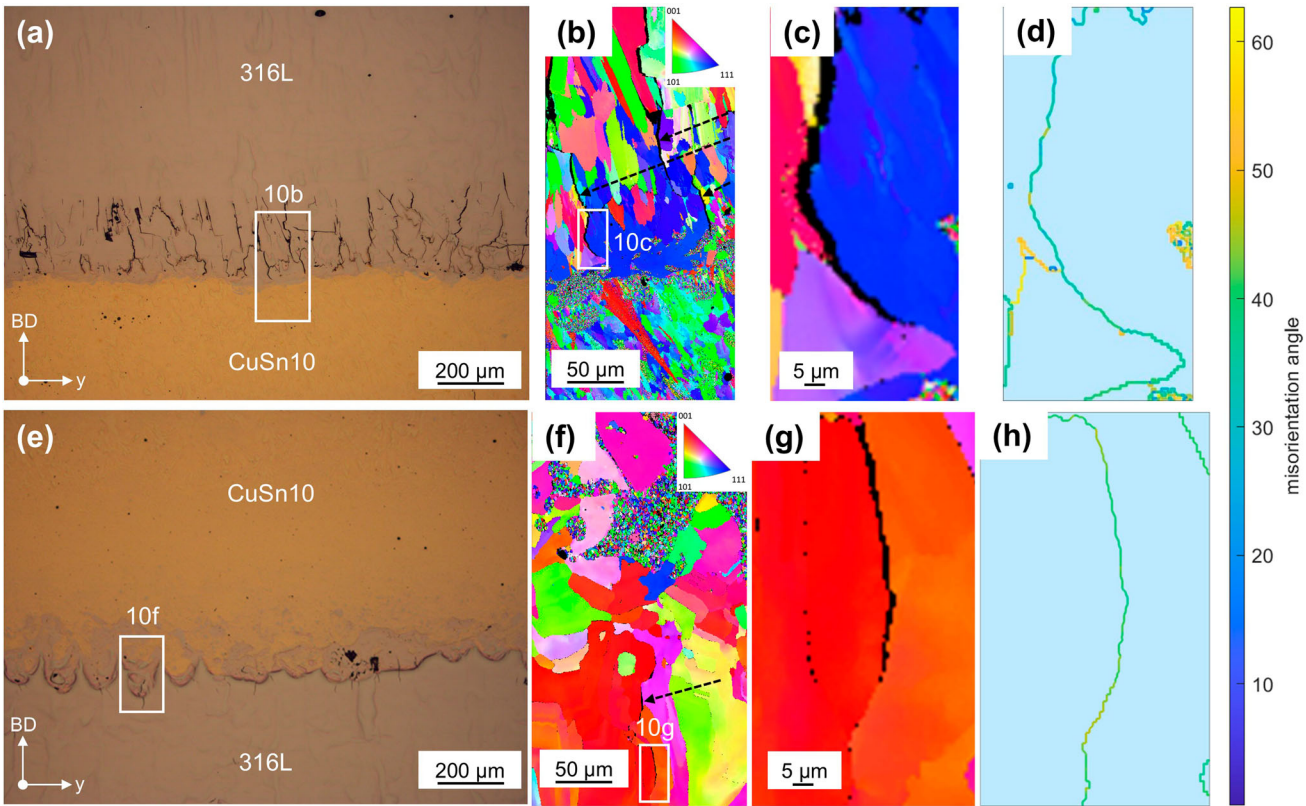


Fig. 10—Crack characterization. (a, e) are optical micrographs of the y-z section of the 316L on top of CuSn10 and CuSn10 on top of 316L samples, respectively. (b, f) represent the IPF map for the section highlighted in (a, e), respectively. (c, g) are a high magnification view of a crack tip in each deposition sequence, with (d, h) showing the related grain boundary misorientation angle maps.

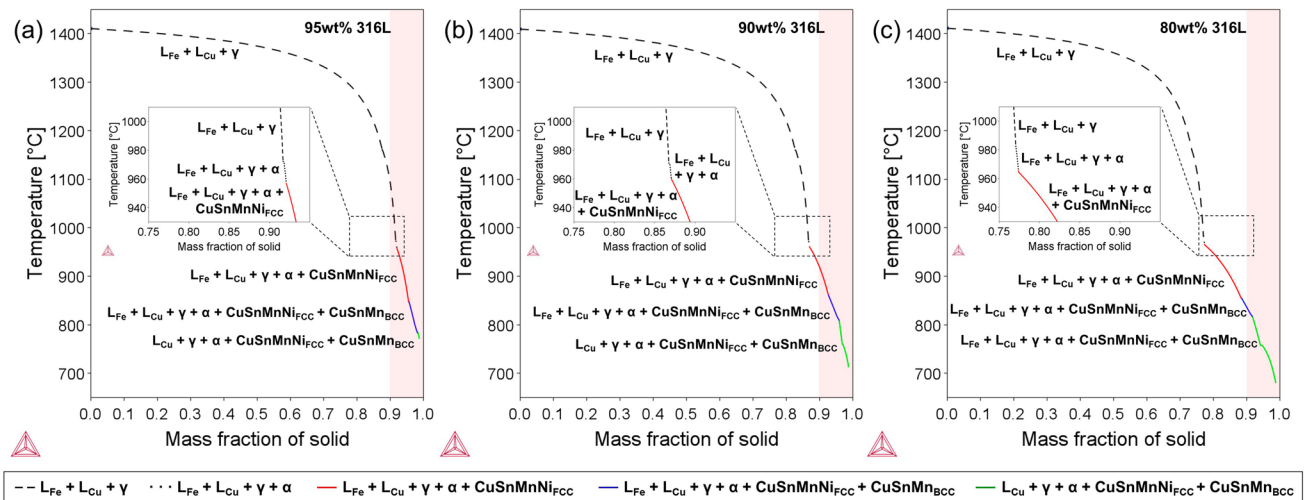


Fig. 11—Solidification path for various 316L-CuSn10 combinations using thermocalc, (a) is 95 wt pct/5 wt pct share of 316L/CuSn10, (b) is 90 wt pct share of 316L, (c) is 80 wt pct share of 316L. The key denotes the phase transformation throughout solidification.

CuSnMnNi phase is reflected by the segregation of Ni to the copper alloy as seen in the EDS maps of Figure 7.

The difference in the solidification temperature of both alloys results in a large solidification range for the melt pool at the interface, alloys which contain a large solidification range like this are susceptible to hot cracking.^[72] A steep gradient is shown in the final

portion of solidification in Figure 11(a) (highlighted by the red region), which is indicative of hot crack susceptibility,^[73] as the remaining liquid metal is insufficient to compensate for the shrinkage which occurs during solidification. This leads to voids forming at the root of the dendrites (due to incomplete liquid filling) which can initiate a crack.^[74] As the CuSn10 content in

the melt pool increases (Figures 11(b) and (c)) the gradient of the solidification path begins to reduce and approaches a melt pool composition which is less likely to be susceptible to hot cracks. The addition of Cu to Fe is widely reported to induce hot cracking, with only a small quantity (< 1 wt pct) of Cu required.^[39,40] Once the material reaches the melting point of Cu, a Cu-rich region of the melt pool forms between the Fe grains, leading to hot cracks. The conduction mode melting of 316L on CuSn10 (appendix Figure 15), results in little mixing of the alloys. Hence, the melt pool at the interface is an Fe-rich liquid with small quantities of Cu liquid intermixed. This is a prime composition for hot cracking. The CuSn10 substrate in this deposition sequence also causes energy to dissipate from the melt pool faster, increasing the cooling rate, and exacerbating the hot crack susceptibility.

On the other hand, studies on the addition of Fe to Cu do not present the same detrimental effect, as is reflected in the CuSn10 sample with a small amount of 316L contamination, shown in Figure 4(e). A study by Li *et al.*^[75] on the effect of cooling rate and iron content on CuFe alloys establishes that a small addition of Fe (> 3 wt pct) into the Cu matrix transforms the grains from columnar to equiaxed. The cooling rate also has a significant effect on the microstructure, with the grain size, whether columnar or equiaxed, reducing as the cooling rate increases. A similar study by Liu *et al.*^[50] found similar results with 8 wt pct Fe, attributing the equiaxed transformation to heterogenous nucleation, increasing the yield strength and ultimate tensile strength considerably. This is observed throughout the interface of CuSn10 on 316L in Figures 6 and 7(e), where the liquid is Cu-rich with small additions of Fe scattered widely across the interface due to the turbulence from the keyhole melting mode, and forming a large area of fine, equiaxed grains (as shown in the appendix Figure 17). As the grain size decreases, the area for the liquid metal to fill will increase, inhibiting crack formation at the grain boundaries.^[30] Smaller grains are also typically better suited to inhibiting crack propagation than coarse grains.^[76] These factors may explain why the deposition sequence of CuSn10 on 316L, with the thick band of fine, equiaxed grains (appendix Figure 17(d)), hinders cracks more readily than the fine strip of equiaxed grains at the interface of 316L on CuSn10 (Figure 10(b)). However, a study by Martendal *et al.*^[23] observed that using a ring beam rather than a gaussian beam reduced cracking when depositing a copper alloy on top of 316L. This method alters the melt pool profile at the interface and significantly reduces mixing of the alloys, preventing the columnar to equiaxed grain transformation. It is unlikely that the mixing will have reduced such that sufficient contamination for hot cracks occurs, as less than 1 wt pct of Cu is needed.^[39,40] Therefore, it is likely that the alteration of the cooling rate from the ring beam profile has a significant effect on the prevention of cracks.

It is clear that the difference in cracking behavior between deposition sequences is complex. However, the difference in heat transfer dynamics and melt pool

behavior between them are key factors in why one deposition sequence suffers from more extensive hot cracking.

Material systems which are susceptible to hot cracking in LPBF conditions can be processed crack-free through manipulation of the process parameters. Altering the process parameters to control the solidification conditions such that solidification speed (R) and temperature gradient (G) are minimised, and therefore strain rates are reduced during solidification, has been shown to successfully reduce cracking in alloys susceptible to hot cracks in LPBF conditions.^[71,77] The application of a second trailing beam to alter the cooling rate at the interface of a Fe and Cu alloy system may show promise in reducing the cooling rate and allow liquid to backfill cracks which develop. However, due to the inevitable mixing of alloys at the interface, and the rapid cooling rate of LPBF, cracking is highly probable. As such, concentrating on the design of the interface and taking advantage of the design flexibility available to AM might be a better solution. This could include incorporating an interlocking feature at the interface which will deflect the fracture path under a tensile load, limiting the impact of hot cracks on the mechanical properties. Such a solution has been demonstrated to be effective between a Ni and Cu alloy.^[78]

The interfacial observations in this study are consistent with other studies which have used a standard LPBF machine and swapped material at some point during the experiment.^[18-20] Therefore, indicating that the interface produced by the Schaeffler Aerosint recoater is equal to that of standard machines and gives confidence in its suitability to investigate multi-material structures with a more advanced interface geometry, such as those shown in Figure 3.

V. CONCLUSION

Bimetallic 316L-CuSn10 samples were produced using LPBF technology with a powder deposition recoater developed by Schaeffler Aerosint, with the goal to understand the formation of the interface and how it is affected by the adopted deposition sequence. A comprehensive investigation of the interface from opposing deposition sequences was conducted to characterize the alloying element distribution, microstructures, phase formation and cracking behavior for both deposition of 316L on top of CuSn10 and CuSn10 on top of 316L. The novel approach taken to corroborate the microscopy images with the XRD depth profiling, and EBSD maps gives a detailed story of the formation of the interface. The main conclusions from this work are summarized as:

1. This manufacturing setup allows printing of individual alloys with near-full density. Both alloys in this work exhibit columnar grains, however, minor contamination of 316L powder particles into the bulk CuSn10 affects the microstructure with fine equiaxed grains distributed throughout the CuSn10 sample. To avoid this, the machine can be

- programmed to momentarily turn off the argon circulation during deposition and continue once the drums have passed the substrate.
2. Deep melt pools, indicative of keyhole melting mode, are visible at the interface when depositing CuSn10 on top of 316L. Subsequently, mixing of the two alloys occurs mainly below the nominal interface, and a wide distribution of circular-shaped ferrite islands. Intergranular cracks are prevalent in the 316L side of the interface.
 3. The conduction melting mode at the interface when depositing 316L on top of CuSn10 produces limited remelting of the underlying CuSn10. A relatively sharp interface forms with no visible melt pools. The limited mixing of the two alloys occurs solely above the nominal interface, with narrow bands of ferrite forming. Intergranular cracks form but are not as widespread as in the opposite deposition sequence. Most of these cracks are backfilled by the copper alloy.
 4. The XRD depth profiling used for identification of the phases throughout the interface provides evidence of ferrite which would go unidentified using traditional XRD methodology in the existing literature. As such, XRD depth profiling is needed to identify potentially detrimental phases which exist at the interface of the bonded 316L and CuSn10 samples in this study.
 5. Experimental measurements of the chemistry and phases at the interface combined with thermodynamic calculations are used to interpret the phases observed at the interface. There is good agreement in the phases present and the segregation of nickel from austenite to the copper matrix between the experiments and the calculations, with the depletion of the austenite-stabilizing nickel content in 316L allowing for the formation of ferrite.
 6. The morphology of the cracking in both deposition sequences are indicative of hot cracks. Similarly, the thermodynamic calculations reflect the hot crack susceptibility (along with the liquid immiscibility and phase formation) of this material combination.
 7. The findings of this study provide results consistent with those which use a standard LPBF machine (and swap material during the experiment). Hence, the Schaeffler Aerosint recoater, despite being responsible for minor cross-contaminations, is a suitable tool for investigating the interfacial properties of multi-material structures with a more complex interface geometry (which requires the 3D spatial material distribution of a purpose-built machine).

ACKNOWLEDGMENTS

The work was supported by the Engineering and Physical Sciences Research Council [Grant Number Ep/V029010/1], Autodesk Research (London, UK), and The Manufacturing Technology Centre (Coventry,

UK). The authors would like to thank the Centre for Additive Manufacturing (CfAM) lab and the Materials lab in Wolfson Building for access to laboratory equipment. The authors also thank the Nanoscale and Microscale Research Centre (nmRC) for providing access to instrumentation.

OPEN ACCESS

This article is licensed under a Creative Commons Attribution 4.0 International License, which permits use, sharing, adaptation, distribution and reproduction in any medium or format, as long as you give appropriate credit to the original author(s) and the source, provide a link to the Creative Commons licence, and indicate if changes were made. The images or other third party material in this article are included in the article's Creative Commons licence, unless indicated otherwise in a credit line to the material. If material is not included in the article's Creative Commons licence and your intended use is not permitted by statutory regulation or exceeds the permitted use, you will need to obtain permission directly from the copyright holder. To view a copy of this licence, visit <http://creativecommons.org/licenses/by/4.0/>.

DATA AVAILABILITY

Data will be made available on request.

COMPETING INTERESTS

The authors declare that they have no known competing financial interests or personal relationships that could have appeared to influence the work reported in this paper.

SUPPLEMENTARY INFORMATION

The online version contains supplementary material available at <https://doi.org/10.1007/s11661-025-07817-1>.

REFERENCES

1. A. Reichardt, A.A. Shapiro, R. Otis, R.P. Dillon, J.P. Borgonia, B.W. McEnerney, P. Hosemann, and A.M. Beese: *Int. Mater. Rev.*, 2021, vol. 66, pp. 1–29. <https://doi.org/10.1080/09506608.2019.1709354>.
2. C. Zhang, F. Chen, Z. Huang, M. Jia, G. Chen, Y. Ye, Y. Lin, W. Liu, B. Chen, Q. Shen, L. Zhang, and E.J. Lavernia: *Mater. Sci. Eng. A*, 2019, <https://doi.org/10.1016/j.msea.2019.138209>.
3. D. Lehmhus, M. Busse, A. Von Hehl, and E. Jäggle, in: *MATEC Web of Conferences, EDP Sciences*, 2018. <https://doi.org/10.1051/mateconf/201818803013>.

4. D.C. Hofmann, J. Kolodziejska, S. Roberts, R. Otis, R.P. Dillon, J.O. Suh, Z.K. Liu, and J.P. Borgonia: *J. Mater. Res.*, 2014, vol. 29, pp. 1899–1910. <https://doi.org/10.1557/jmr.2014.208>.
5. Y. Fang, X. Jiang, D. Mo, D. Zhu, and Z. Luo: *Int. J. Adv. Manuf. Technol.*, 2019, vol. 102, pp. 2845–63. <https://doi.org/10.1007/s00170-019-03353-6>.
6. S.M. de Carvalho, R.H.M. Siqueira, and M.S.F. de Lima: *J. Aerosp. Technol. Manag.*, 2019, <https://doi.org/10.5028/jatm.v11.1083>.
7. J. Kar, S.K. Roy, and G.G. Roy: *J. Mater. Process. Technol.*, 2016, vol. 233, pp. 174–85. <https://doi.org/10.1016/j.jmatprotec.2016.03.001>.
8. H.S. Lee, J.H. Yoon, J.T. Yoo, and Y.M. Yi: *Materwiss Werksttech*, 2011, vol. 42, pp. 985–89. <https://doi.org/10.1002/mawe.201100856>.
9. H.D. Vyas, K.P. Mehta, V. Badheka, and B. Doshi: *Mater. Sci. Eng. A*, 2022, <https://doi.org/10.1016/j.msea.2021.142444>.
10. T. DebRoy, H.L. Wei, J.S. Zuback, T. Mukherjee, J.W. Elmer, J.O. Milewski, A.M. Beese, A. Wilson-Heid, A. De, and W. Zhang: *Prog. Mater. Sci.*, 2018, vol. 92, pp. 112–224. <https://doi.org/10.1016/j.pmatsci.2017.10.001>.
11. M. Ribeiro, O. Sousa Carneiro, and A. Ferreira da Silva: *Rapid Prototyp. J.*, 2019, vol. 25, pp. 38–46. <https://doi.org/10.1108/RPJ-05-2017-0107>.
12. C. Wei and L. Li: *Virtual Phys. Prototyp.*, 2021, vol. 16, pp. 347–71. <https://doi.org/10.1080/17452759.2021.1928520>.
13. C. Wei, L. Li, X. Zhang, and Y.H. Chueh: *CIRP Ann.*, 2018, vol. 67, pp. 245–48. <https://doi.org/10.1016/j.cirp.2018.04.096>.
14. A.G. Demir and B. Previtali: *Manuf. Lett.*, 2017, vol. 11, pp. 8–11. <https://doi.org/10.1016/j.mfglet.2017.01.002>.
15. B. Neirincx, X. Li, and M. Hick: *Acc. Mater. Res.*, 2021, vol. 2, pp. 387–93. <https://doi.org/10.1021/accountsmr.1c00030>.
16. X. Li, D. Sukhomlinov, and Z. Que: *Int. J. Miner. Metall. Mater.*, 2024, vol. 31, pp. 118–28. <https://doi.org/10.1007/s12613-023-2747-x>.
17. M. Oel, J. Rossmann, B. Bode, I. Meyer, T. Ehlers, C.M. Hackl, and R. Lachmayer: *Addit. Manuf. Lett.*, 2023, <https://doi.org/10.1016/j.addlet.2023.100165>.
18. X. Wang, Z. Liu, Y. Tao, Y. Zhou, S. Wen, and Y. Shi: *Addit. Manuf.*, 2023, <https://doi.org/10.1016/j.addma.2023.103860>.
19. K. Chen, C. Wang, Q. Hong, S. Wen, Y. Zhou, C. Yan, and Y. Shi: *J. Mater. Process. Technol.*, 2020, <https://doi.org/10.1016/j.jmatprotec.2020.116701>.
20. C. Tan, Y. Chew, G. Bi, D. Wang, W. Ma, Y. Yang, and K. Zhou: *J. Mater. Sci. Technol.*, 2021, vol. 72, pp. 217–22. <https://doi.org/10.1016/j.jmst.2020.07.044>.
21. J. Chen, Y. Yang, C. Song, D. Wang, S. Wu, and M. Zhang: *Mater. Sci. Eng. A*, 2020, <https://doi.org/10.1016/j.msea.2020.139316>.
22. J. Chen, M. Zhang, D. Zhao, G. Bi, Y. Bai, Y. Xiao, and D. Wang: *Mater. Charact.*, 2024, <https://doi.org/10.1016/j.matchar.2024.113862>.
23. C.P. Martendal, P.D.B. Esteves, L. Deillon, F. Malamud, A.M. Jamili, J.F. Löffler, and M. Bambach: *J. Mater. Process. Technol.*, 2024, vol. 327, 118344 <https://doi.org/10.1016/j.jmatprotec.2024.118344>.
24. O.M. Al-Jamal, S. Hinduja, and L. Li: *CIRP Ann. Manuf. Technol.*, 2008, vol. 57, pp. 239–42. <https://doi.org/10.1016/j.cirp.2008.03.010>.
25. Y.Z. Chen, F. Liu, G.C. Yang, X.Q. Xu, and Y.H. Zhou: *J. Alloys Compd.*, 2007, <https://doi.org/10.1016/j.jallcom.2006.03.012>.
26. S. Chen, X. Yu, J. Huang, J. Yang, and S. Lin: *J. Alloys Compd.*, 2019, vol. 773, pp. 719–29. <https://doi.org/10.1016/j.jallcom.2018.09.282>.
27. Y. Wen, X. Wu, A. Huang, R.L. Narayan, P. Wang, L. Zhang, B. Zhang, U. Ramamurty, and X. Qu: *Acta Mater.*, 2024, <https://doi.org/10.1016/j.actamat.2023.119572>.
28. Y. Bai, J. Zhang, C. Zhao, C. Li, and H. Wang: *Mater. Charact.*, 2020, <https://doi.org/10.1016/j.matchar.2020.110489>.
29. J. Chen, Y. Yang, D. Wang, Z. Liu, and C. Song: *Mater. Lett.*, 2021, <https://doi.org/10.1016/j.matlet.2021.129377>.
30. J.E. Norkett, M.D. Dickey, and V.M. Miller: *Metall. Mater. Trans. A.*, 2021, vol. 52A, pp. 2158–72. <https://doi.org/10.1007/s11661-021-06256-y>.
31. C. Rock, P. Tarafder, L. Ives, and T. Horn: *Mater. Des.*, 2021, <https://doi.org/10.1016/j.matdes.2021.110278>.
32. Z.H. Liu, D.Q. Zhang, S.L. Sing, C.K. Chua, and L.E. Loh: *Mater. Charact.*, 2014, vol. 94, pp. 116–25. <https://doi.org/10.1016/j.matchar.2014.05.001>.
33. W. Zhang, H. Liao, Z. Hu, S. Zhang, B. Chen, H. Yang, Y. Wang, and H. Zhu: *J. Mater. Sci. Technol.*, 2021, vol. 90, pp. 121–32. <https://doi.org/10.1016/j.jmst.2021.03.008>.
34. C. Shanjeevi, S. Satish Kumar, and P. Sathiyar: *Proc. Inst. Mech. Eng. B J. Eng. Manuf.*, 2014, vol. 230, pp. 449–57. <https://doi.org/10.1177/0954405414555590>.
35. K. Tsuchiya and H. Kawamura: *J. Nucl. Mater.*, 1996, vol. 233–237, pp. 913–17. [https://doi.org/10.1016/S0022-3115\(96\)00104-3](https://doi.org/10.1016/S0022-3115(96)00104-3).
36. A. Zafari and K. Xia: *Addit. Manuf.*, 2021, <https://doi.org/10.1016/j.addma.2021.102270>.
37. W.R. Kim, G.B. Bang, J.H. Park, T.W. Lee, B.S. Lee, S.M. Yang, G.H. Kim, K. Lee, and H.G. Kim: *J. Market. Res.*, 2020, vol. 9, pp. 12834–39. <https://doi.org/10.1016/j.jmrt.2020.09.051>.
38. M.R. Tucker, L. Deillon, R. Forner, and M. Bambach: *Prog. Addit. Manuf.*, 2024, <https://doi.org/10.1007/s40964-024-00674-1>.
39. L.G. Garza and C.J. Van Tyne: *J. Mater. Process. Technol.*, 2005, vol. 159, pp. 169–80. <https://doi.org/10.1016/j.jmatprotec.2004.05.004>.
40. N. Imai, N. Komatsubara, and K. Kunishige: *ISIJ Int.*, 1997, vol. 37, pp. 224–31. <https://doi.org/10.2355/isijinternational.37.224>.
41. Z. Li, Z. Kuai, B. Liu, Y. Chen, H. Li, Y. Wang, W. Huo, M. Wei, H. Yang, and P. Bai: *J. Market. Res.*, 2023, vol. 25, pp. 3819–34. <https://doi.org/10.1016/j.jmrt.2023.06.196>.
42. L. Deillon, N. Abando Beldarrain, X. Li, and M. Bambach: *Mater. Des.*, 2024, <https://doi.org/10.1016/j.matdes.2024.112914>.
43. J. Chen, Y. Yang, C. Song, M. Zhang, S. Wu, and D. Wang: *Mater. Sci. Eng. A*, 2019, vol. 752, pp. 75–85. <https://doi.org/10.1016/j.msea.2019.02.097>.
44. G. Telasang, S. Narayanaswamy, D.M. Santhoshsarang, and R. Bathe: *J. Manuf. Process.*, 2022, vol. 80, pp. 920–29. <https://doi.org/10.1016/j.jmapro.2022.06.055>.
45. S. Mao, D.Z. Zhang, Z. Ren, G. Fu, and X. Ma: *J. Alloys Compd.*, 2022, <https://doi.org/10.1016/j.jallcom.2021.163256>.
46. L. Liu, D. Wang, C. Han, Y. Li, T. Wang, Y. Wei, W. Zhou, M. Yan, Y. Liu, S. Wei, and Y. Yang: *J. Alloys Compd.*, 2024, <https://doi.org/10.1016/j.jallcom.2024.173508>.
47. M. Schneck, M. Horn, M. Schmitt, C. Seidel, G. Schlick, and G. Reinhart: *Prog. Addit. Manuf.*, 2021, vol. 6, pp. 881–94. <https://doi.org/10.1007/s40964-021-00205-2>.
48. Y.M. Mos, A.C. Vermeulen, C.J.N. Buisman, and J. Weijma: *Geomicrobiol. J.*, 2018, vol. 35, pp. 511–17. <https://doi.org/10.1080/01490451.2017.1401183>.
49. J.-O. Andersson, T. Helander, L. Höglund, P. Shi, and B. Sundman: *Calphad*, 2002, vol. 26, pp. 273–312. [https://doi.org/10.1016/S0364-5916\(02\)00037-8](https://doi.org/10.1016/S0364-5916(02)00037-8).
50. Y. Liu, J. Zhang, Q. Sun, M. Li, M. Yan, X. Cheng, M. Li, and M.X. Zhang: *J. Mater. Sci. Technol.*, 2023, vol. 134, pp. 50–59. <https://doi.org/10.1016/j.jmst.2022.06.007>.
51. I. Meyer, M. Oel, T. Ehlers, and R. Lachmayer: *Heliyon*, 2023, <https://doi.org/10.1016/j.heliyon.2023.e18301>.
52. R.P. Shi, C.P. Wang, D. Wheeler, X.J. Liu, and Y. Wang: *Acta Mater.*, 2013, vol. 61, pp. 1229–43. <https://doi.org/10.1016/j.actamat.2012.10.033>.
53. S. Curitto, R. Greco, N.H. Pryds, E. Johnson, and L. Battezzati: *Fluid Phase Equilib.*, 2007, vol. 256, pp. 132–36. <https://doi.org/10.1016/j.fluid.2006.10.003>.
54. D. Wang, C. Song, Y. Yang, and Y. Bai: *Mater. Des.*, 2016, vol. 100, pp. 291–99. <https://doi.org/10.1016/j.matdes.2016.03.111>.
55. K. Saeidi, X. Gao, Y. Zhong, and Z.J. Shen: *Mater. Sci. Eng. A*, 2015, vol. 625, pp. 221–29. <https://doi.org/10.1016/j.msea.2014.12.018>.
56. Y. Zhou, Y. Fang, J. Wang, L. Xu, and D. Wang: *J. Phys. Conf. Ser. Inst. Phys.*, 2022, <https://doi.org/10.1088/1742-6596/2262/1/012002>.
57. S. Scudino, C. Unterdörfer, K.G. Prashanth, H. Attar, N. Ellendt, V. Uhlenwinkel, and J. Eckert: *Mater. Lett.*, 2015, vol. 156, pp. 202–04. <https://doi.org/10.1016/j.matlet.2015.05.076>.
58. M. Chen, S. van Petegem, Z. Zou, M. Simonelli, Y.Y. Tse, C.S.T. Chang, M.G. Makowska, D. Ferreira Sanchez, and H.

- Moens-Van Swygenhoven: *Addit. Manuf.*, 2022. <https://doi.org/10.1016/j.addma.2022.103173>.
59. N. Ahmed, I. Barsoum, G. Haidemenopoulos, and R.K.A. Al-Rub: *J. Manuf. Process.*, 2022, vol. 75, pp. 415–34. <https://doi.org/10.1016/j.jmapro.2021.12.064>.
 60. M.P. Haines, M.S. Moyle, V.V. Rielli, V. Luzin, N. Haghdadi, and S. Primig: *Addit. Manuf.*, 2023, <https://doi.org/10.1016/j.addma.2023.103686>.
 61. H.E. Sabzi, S. Maeng, X. Liang, M. Simonelli, N.T. Aboulkhair, and P.E.J. Rivera-Diaz-del-Castillo: *Addit. Manuf.*, 2020, <https://doi.org/10.1016/j.addma.2020.101360>.
 62. P.S. Korinko and S.H. Malene: *Pract. Fail. Anal.*, 2001, vol. 1, pp. 61–68. <https://doi.org/10.1007/BF02715336>.
 63. M. Qu, J. Yuan, A. Nabaa, J. Huang, C.A. Chuang, and L. Chen: *Acta Mater.*, 2024, <https://doi.org/10.1016/j.actamat.2024.119875>.
 64. L. Yao, S. Huang, U. Ramamurty, and Z. Xiao: *Acta Mater.*, 2021, <https://doi.org/10.1016/j.actamat.2021.117331>.
 65. E.F. Nippes and D.J. Ball: *Copper Contamination Cracking: Cracking Mechanism and Crack Inhibitors: Final Report*, International Copper Research Association, Rensselaer Polytechnic Institute, Department of Materials Engineering, 1980. <https://books.google.co.uk/books?id=R0J6HAAACAAJ>.
 66. S. Chen, J. Huang, J. Xia, H. Zhang, and X. Zhao: *Metall. Mater. Trans. A Phys. Metall. Mater. Sci.*, 2013, vol. 44A, pp. 3690–96. <https://doi.org/10.1007/s11661-013-1693-z>.
 67. J. Gao, C. Li, C. Guo, and Z. Du: *Int. J. Miner. Metall. Mater.*, 2019, vol. 26, pp. 1427–35. <https://doi.org/10.1007/s12613-019-1798-5>.
 68. J. Chen, Y. Yang, Y. Bai, D. Wang, C. Zhao, and J. Ying His Fuh: *Mater. Charact.*, 2022, <https://doi.org/10.1016/j.matchar.2021.111654>.
 69. S. Rao and A.Y. Al-Kawaie: *Weld. J.*, 2010, vol. 89, pp. 46–49.
 70. A. Sonawane, G. Roux, J.J. Blandin, A. Despres, and G. Martin: *Materialia (Oxf.)*, 2021, <https://doi.org/10.1016/j.mtla.2020.100976>.
 71. G. Del Guercio, D.G. McCartney, N.T. Aboulkhair, S. Robertson, R. Maclachlan, C. Tuck, and M. Simonelli: *Addit. Manuf.*, 2022, <https://doi.org/10.1016/j.addma.2022.102776>.
 72. G.K. Sigworth: *Hot Tearing of Metals*, Alcoa Inc, New York, 2002.
 73. S. Kou: *Acta Mater.*, 2015, vol. 88, pp. 366–74. <https://doi.org/10.1016/j.actamat.2015.01.034>.
 74. M. Rappaz, J.-M. Drezet, and M. Gremaud: *Metall. Mater. Trans. A.*, 1999, <https://doi.org/10.1007/s11661-999-0334-z>.
 75. B. Li, H. Zhang, and J. Cui: *Adv. Mater. Res.*, 2011, <https://doi.org/10.4028/www.scientific.net/AMR.327.89>.
 76. J.H. Martin, B.D. Yahata, J.M. Hundley, J.A. Mayer, T.A. Schaedler, and T.M. Pollock: *Nature*, 2017, vol. 549, pp. 365–69. <https://doi.org/10.1038/nature23894>.
 77. S. Bergmueller, J. Scheiber, L. Kaserer, and G. Leichtfried: *Addit. Manuf.*, 2023, <https://doi.org/10.1016/j.addma.2023.103727>.
 78. L. Liu, D. Wang, T. Wang, C. Han, Y. Li, H. Tan, W. Zhou, X. Yan, L. Lei, and Y. Yang: *Int. J. Mach. Tools Manuf.*, 2025, <https://doi.org/10.1016/j.ijmachtools.2024.104236>.

Publisher's Note Springer Nature remains neutral with regard to jurisdictional claims in published maps and institutional affiliations.